Feature Extraction of Micro-Motional Targets via Time-Range Distribution

XIAOFENG AI [ID], ZHIMING XU [ID], AND FENG ZHAO

State Key Laboratory of Complex Electromagnetic Environmental Effects on Electronics and Information System, National University of Defense Technology, Changsha 410073, China

Corresponding author: Zhiming Xu (376644944@qq.com)

ABSTRACT The micro-motional period is an important feature for spatial target discrimination. Firstly, the movement and wideband echo models of wobbling targets with bistatic observations are introduced. Then, the characteristics of the mono-/bi-static high-resolution range profiles (HRRPs) with different polarizations are analyzed based on the simulation echoes of the wobbling target via the electromagnetic calculations. Finally, the observed HRRP sequence is employed to construct a time-range distribution matrix, and an estimation method of the micro-motional period is proposed based on the time-range distribution matrix correlation, which is validated by the measurement experiments in the anechoic chamber.

INDEX TERMS Micro-motion, bistatic radar, time-range distribution, feature extraction.

I. INTRODUCTION

Bistatic radar with the separated transmitter and receiver configuration offers the ability to detect stealthy targets and the immunity to jamming [1], [2]. In recent years, a great deal of literatures about bistatic system experiments, such as passive radar, bistatic SAR and ISAR, are published which means that the advantages of bistatic radar have been utilized in the real applications [3]–[5].

Spatial targets maintain stability by rapid spinning and a precession occurs if the spinning is disturbed by an external interference [6]. Without attitude control, these targets will generate wobbling or tumbling, which can be utilized to effectively distinguish targets. This precession feature has been used for spatial target recognition, and many effective methods for precession feature extraction have been proposed and validated by experimental data [6]–[10]. In recent years, characteristics analysis, feature extraction and recognition of wobbling targets have gained worldwide attention [11]–[14]. The current wobbling micro-motion models are mainly based on the localized scattering center model which assume the scattering center location remains unchanged with the line of sight (LOS) varying. These models are only suitable for the slot, and wing components of cone-shaped targets. Whereas the scattering centers existing on the bottom edge of the cone-shaped targets are sliding with LOS variation

and deviate this scattering mechanism. The existing models cannot adapt to this situation and should be improved.

In recent years, characteristics analysis and feature extraction of micro-motion targets in bistatic radar have attracted significant attention [15]–[18]. Although feature extraction methods of vibrating, rotational and precession targets in bistatic radar have been developed, the bistatic micro-motion characteristics of wobbling targets have not been investigated enough. This paper focuses on the bistatic wideband echo models of wobbling targets and considers how to utilize bistatic high-resolution range profiles (HRRPs) for feature extraction.

The remainder of this paper is organized as follows: Section 2 introduces the bistatic observation model of the wobbling target. Section 3 constructs a time-range distribution matrix with a bistatic HRRP sequence and introduces a period estimation method based on the time-range distribution matrix correlation. Section 4 shows dynamic simulation results with electromagnetic calculation data. Section 5 validates the proposed method by experimental data. Section 6 gives the conclusion.

II. BISTATIC MICRO-MOTION MODEL OF WOBBLING TARGETS

As shown in Fig. 1, for a rotational symmetry cone-shaped target, the bistatic scattering centers are marked as A, B and C, in the plane that is constructed by the symmetry
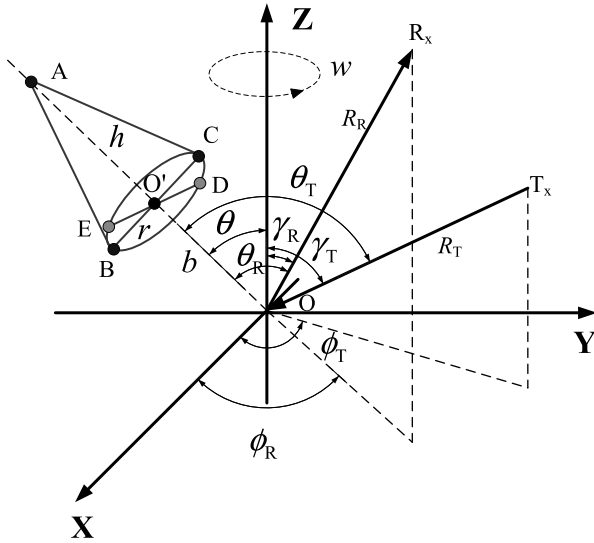
FIGURE 1. Geometry of wobbling targets.

axis and the bisector of the bistatic angle [19]. The monostatic scattering centers are marked as A, D and E, in the plane constructed by the symmetry axis and the radar LOS [7].

Fig. 1 shows the geometry coordinates, where the origin O is positioned on the symmetry axis. The transmitter and the receiver are located at T_x and R_x, respectively. The elevation and azimuth angles of LOS of the transmitter are denoted as γ_T and ϕ_T. The elevation and azimuth angles of LOS of the receiver are denoted as γ_R and ϕ_R. The cone height is h, and the radius of the cone base is r. The length of OO' is b and the bistatic distance of the origin O is R_S. Assume that the target wobbles in the YOZ plane and that the maximum wobbling angle is θ_0. The wobbling speed and period are ω and T_w, respectively. Hence, the wobbling angle is $\theta = \theta_0 \sin(\omega t)$.

With the target wobbling, the angle $\angle T_x OA$, denoted as θ_T, changes as follows

$$\cos \theta_T = \cos \gamma_T \cos (\theta_0 \sin \omega t) + \sin \gamma_T \sin \phi_T \sin (\theta_0 \sin \omega t) \tag{1}$$

Similarly, the angle $\angle R_x OA$ denoted as θ_R changes as follows

$$\cos \theta_R = \cos \gamma_R \cos (\theta_0 \sin \omega t) + \sin \phi_R \sin \gamma_R \sin (\theta_0 \sin \omega t) \tag{2}$$

The bistatic angle β satisfies

$$\cos \beta = \cos \gamma_T \cos \gamma_R + \sin \gamma_T \sin \gamma_R \cos \phi_R \cos \phi_T$$
$$+ \sin \gamma_T \sin \gamma_R \sin \phi_R \sin \phi_T \tag{3}$$

Thus, the following equation is obtained.

$$\cos \beta/2 = \sqrt{\frac{\begin{array}{l} 1 + \cos \gamma_T \cos \gamma_R + \sin \gamma_T \sin \gamma_R \cos \phi_R \cos \phi_T \\ + \sin \gamma_T \sin \gamma_R \sin \phi_R \sin \phi_T \end{array}}{2}} \tag{4}$$

And the angle between the target axis and the bisector of the bistatic angle, denoted as θ_{Bi}, satisfies

$$\cos \theta_{Bi} = \frac{(\cos \theta_R + \cos \theta_T)}{2 \cos \beta/2} \tag{5}$$

At t, the bistatic distance of scattering center A is

$$\begin{aligned} R_{S_A} &\approx R_T + R_R - (h + b)(\cos \theta_T + \cos \theta_R) \\ &= R_T + R_R - (b + h) \cos \beta/2 \cos \theta_{Bi} \\ &= R_S - (b + h) \cos \beta/2 \cos \theta_{Bi} \end{aligned} \tag{6}$$

Then, the bistatic distance of scattering center B is

$$\begin{aligned} R_{S_B} &\approx R_R + R_T - b (\cos \theta_R + \cos \theta_T) \\ &\quad + r\sqrt{\sin^2 \theta_T + 2(\cos \beta - \cos \theta_T \cos \theta_R) + \sin^2 \theta_R} \\ &= R_R + R_T - 2\cos \beta/2 (b \cos \theta_{Bi} - r \sin \theta_{Bi}) \\ &= R_S - 2\cos \beta/2 (b \cos \theta_{Bi} - r \sin \theta_{Bi}) \end{aligned} \tag{7}$$

Similarly, the bistatic distance of scattering center C is

$$\begin{aligned} R_{S_C} &\approx R_R + R_T - b (\cos \theta_R + \cos \theta_T) \\ &\quad + r\sqrt{\sin^2 \theta_T + 2(\cos \beta - \cos \theta_T \cos \theta_R) + \sin^2 \theta_R} \\ &= R_R + R_T - 2\cos \beta/2 (b \cos \theta_{Bi} - r \sin \theta_{Bi}) \\ &= R_S - 2\cos \beta/2 (b \cos \theta_{Bi} - r \sin \theta_{Bi}) \end{aligned} \tag{8}$$

Eq. (6), (7) and (8) express the movement rule of each scattering center. Each scattering center moves with a complex rule, which is not same as the typical sinusoidal rule in the monostatic configuration. It can be considered as the sum of many sine functions.

Taking the reference distance $\Delta R_{Si} = R_{Si} - R_S$ in consideration, the following bistatic distances are defined as

$$\begin{cases} \Delta R_{S_A} \approx -\cos \beta/2 (b + h) \cos \theta_{Bi} \\ \Delta R_{S_B} \approx -\cos \beta/2 (b \cos \theta_{Bi} - r \sin \theta_{Bi}) \\ \Delta R_{S_C} \approx -\cos \beta/2 (b \cos \theta_{Bi} + r \sin \theta_{Bi}) \end{cases} \tag{9}$$

where $\Delta R_{S_A}, \Delta R_{S_B}$, and ΔR_{S_C} denotes the reference distances of bistatic scattering centers A, B and C, respectively. Eq. (9) shows that all bistatic scattering centers move with a complex rule when the target is wobbling. If $\theta_R = \theta_T$, $\phi_R = \phi_T$, Eq. (9) corresponds to the monostatic case, which can be expressed as

$$\begin{cases} \Delta R_{T_A} \approx -(b + h) \cos \theta_T \\ \Delta R_{T_D} \approx -(b \cos \theta_T - r \sin \theta_T) \\ \Delta R_{T_E} \approx -(b \cos \theta_T + r \sin \theta_T) \end{cases} \tag{10}$$

where $\Delta R_{T_A}, \Delta R_{T_D}$, and ΔR_{T_E} denote the reference distances of scattering centers A, D, and E respectively.

The comparison of (9) with (10) reveals that the bistatic observed rules are identical to the monostatic radar on the bisector of the bistatic angle. Although the monostatic receiver and the bistatic receiver observe different scattering centers, identical movement and structure parameters are included in the observed information.

III. BISTATIC TIME-RANGE DISTRIBUTION AND PERIOD ESTIMATION

Without loss of generality, the linear frequency modulated (LFM) signal is used in this paper.

$$s(t_m, \hat{t}) = \text{rect}\left(\frac{\hat{t}}{T}\right) \exp\left[j2\pi\left(f_0 t + \frac{1}{2}k\hat{t}^2\right)\right] \quad (11)$$

where $\text{rect}(t) = \begin{cases} 1 & |t| < 1/2 \\ 0 & \text{else} \end{cases}$, f_0 is the carrier frequency, T is the pulse width, k is the chirp rate, $\hat{t}$ is the fast time, and t_m is the slow time. The full time is $t = \hat{t} + t_m$.

The bistatic HRRP can be obtained via stretch processing and range compressing at the slow time t_m as the same process method in the monostatic case.

$$S(t_m, f) = T\sum \sigma_i \text{sinc}\left[T\left(f + \frac{2k}{c}\Delta R_{S_i}(t_m)\right)\right] e^{j2\pi f_0 \frac{2\Delta R_{S_i}(t_m)}{c}} \quad (12)$$

where $\Delta R_{S_i}(t_m)$ expresses the range sum of the ith bistatic scattering center, and σ_i expresses the scattering amplitude of the ith bistatic scattering center.

The amplitude of $S(t_m, f)$ can be expressed as

$$H(t_m, r) = T\sum_i \sigma_i \cdot \text{sinc}\left[\frac{2B}{c}\left(r - \Delta R_{S_i}(t_m)\right)\right] \quad (13)$$

The correlation coefficients of the range profile at t_k and the first range profile at t_1 can be expressed as [20], [21]

$$\mathbf{C}(k, \Delta r) = \max\left\{\int H(t_1, r) H^*(t_k, r + \Delta r) dr\right\} \quad (14)$$

where $k = 1 \sim N$ and N denotes the pulse number.

Taking the scattering center A in (10) as an example, ΔR_{T_A} can be expressed as

$$\Delta R_{T_A}(t) \approx -(h + b)A_0 \cos(\theta_0 \sin\omega t - \psi) \quad (15)$$

where $A_0 = \sqrt{\cos^2\gamma_T + \sin^2\gamma_T \sin^2\phi_T}$, $\text{tg}\psi = \frac{\sin\gamma_T \sin\phi_T}{\cos\gamma_T}$.

Acording to (15), a peak value in the one-dimensional profile will appear at $\Delta R_{T_A}(0) \approx -(h + b)A_0 \cos\psi$ when $t = 0$. Maybe several peak values exist in a wobbling period.

Let $\Delta R_{T_A}(t) = \Delta R_{T_A}(0)$, then $\cos(\theta_0\sin\omega t - \psi) = \cos\psi$, which indicates that $2n\pi \pm \psi = \theta_0\sin\omega t - \psi$, s.t. $\theta_0\sin\omega t = \begin{cases} 0 \\ 2n\pi + 2\psi \end{cases}$.

If $\theta_0\sin\omega t = 0$, then $t = 0, \frac{\pi}{\omega}$. If $\theta_0\sin\omega t = 2n\pi + 2\psi$, a specific time makes this equation true only if $\theta_0 \geq |2n\pi + 2\psi|$. And the following solution can be obtained.

$$t = \begin{cases} \frac{1}{\omega}a\sin\left(\frac{2\psi}{\theta_0}\right), & \frac{1}{\omega}\pi - a\sin\left(\frac{2\psi}{\theta_0}\right) & \theta_0 \geq 2\psi \\ \frac{1}{\omega}\left[\pi + a\sin\left(\frac{-2\pi + 2\psi}{\theta_0}\right)\right], & \\ \frac{1}{\omega}\left[2\pi - a\sin\left(\frac{-2\pi + 2\psi}{\theta_0}\right)\right], & \theta_0 \geq 2\pi - 2\psi \end{cases} \quad (16)$$

So several peak values exist in a wobbling period. Similarly, other scattering centers also obey these rules in both the monostatic case (D and E) and the bistatic case (B and C). At least one range profile will be the same as the range profile at time t = 0 in one wobbling period. The peak value of the correlation coefficients will appear at the integral times of a half wobbling period or other time, which means that the estimated wobbling period via the peak value detection will not be right. What's more, this method is affected by the target scattering characteristics, the micro-motion amplitude and the signal bandwidth and a false period value is easily produced.

Assuming that the observation time is longer than one wobbling period, the time-range distribution matrix is expressed as

$$\mathbf{M}(t_m, r) = \{H(t_1, r), H(t_2, r), \cdots, H(t_M, r)\} \quad (17)$$

According to (9) and (13), $H(t_m, r) = H(t_m + T_w, r)$; thus, $\mathbf{M}(t_m, r) = \mathbf{M}(t_m + T_w, r)$. The two-dimensional autocorrelation of the time-range distribution matrix $\mathbf{M}(t_m, r)$ can be expressed as

$$\mathbf{C}(\Delta t, \Delta r) = \iint \mathbf{M}(t_m, r)\mathbf{M}^H(t_m + \Delta t, r + \Delta r) dr dt_m \quad (18)$$

Then, the peak value of the correlation matrix $\mathbf{C}(\Delta t, \Delta r)$ should appear at $n \cdot T_w$, which denotes n times of the wobbling period. Because (18) utilizes all profiles for the correlation calculation, the false peak values that appear in (14) are greatly reduced compared with the correlation method of the single range profile. Thus, its robustness is improved. Assuming the pulse repetition frequency (PRF) is f_r, the time resolution of the correlation matrix is $1/f_r$. Because the maximum error of the peak position is half of the time resolution, the maximum wobble period estimated error is $1/2f_r$. Consequently, the period estimation accuracy is dependent on the time resolution.

IV. ELECTROMAGNETIC COMPUTATION AND SIMULATION

The scattering filed (both monostatic and bistatic case) of a cone-shaped model, as shown in Fig. 2, is obtained by CST, a generic electromagnetic calculation software. The electro-magnetic calculation frequency is 9.5~10.5 GHz with 10 MHz internal. The incident azimuth angle is set as 0°. The incident elevation, scattering elevation and azimuth angle are all 0~180° with 0.2° internal. The incident polarization is only horizontal, while the receiving polarization includes both horizontal and vertical. With the electromagnetic computation data, the dynamic monostatic and bistatic HRRP with target wobbling can be simulated. The simulation parameters are as follows: $\theta_0 = 20°$ and $\omega = 2\pi$ rad/s. The pulse repetition frequency (PRF) is set as 500 Hz, and the observation time is 2 s.

The simulation flow is described as follows. Firstly, the aspect angles relative to the LOS of the transmitter and
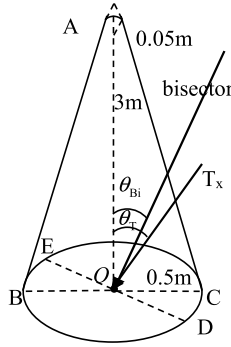
FIGURE 2. Target model for electromagnetic calculation.

receiver are calculated. Then, both the bistatic and monostatic scattering field corresponding to these angles are extracted from the electromagnetic data calculated via CST. And then, the white Gauss noises (WGNs) are added to the bistatic and monostatic scattering field. Finally, the bistatic and monostatic HRRPs are obtained by taking the inverse fast Fourier transform (IFFT) on the above data. According to (17), the time-range distribution matrix **M** is finally obtained.
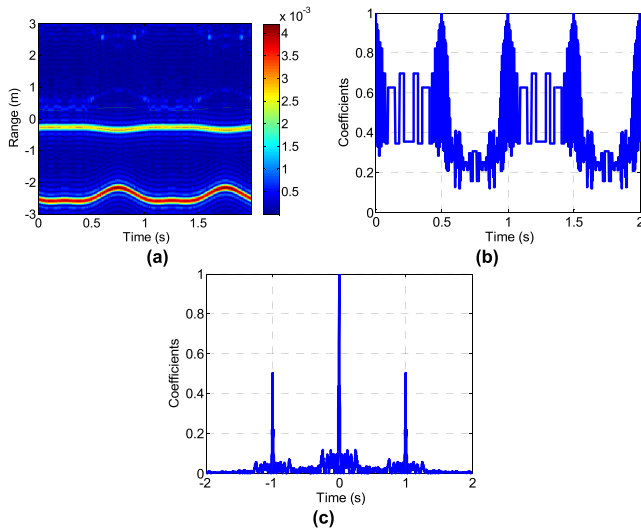
FIGURE 3. Monostatic time-range distribution and period estimation (HH polarization, $\gamma_T = 35°$, $\varphi_T = 20°$). (a) time-range distribution. (b) correlation coefficients of single range profile(c) matrix correlation coefficients at $\Delta r = 0$.

The monostatic time-range distribution images and the correlation coefficients with the parameters $\gamma_T = 35°$ and $\varphi_T = 20°$ are shown in Fig. 3 and Fig.4: (a) shows the time-range distribution images, and the dashed lines represent the reference distances of the three scattering centers that is calculated via (10). The range-time distribution images show that the theoretical curves are consistent with the traces of the observed scattering centers. Due to target self-occlusion, only the two scattering centers A and D can be observed, which cannot completely describe the target. For horizontal-vertical (HV) polarization, the monostatic scattering coefficients are substantially smaller (approximately
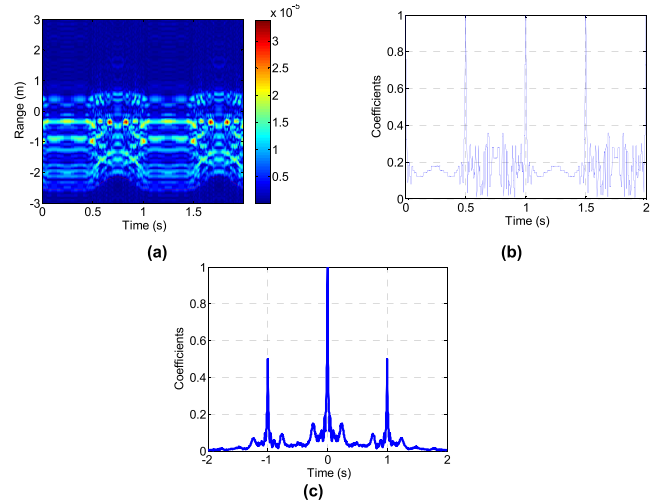

FIGURE 4. Monostatic time-range distribution and period estimation (HV polarization, $\gamma_T = 35°$, $\varphi_T = 20°$). (a) time-range distribution. (b) correlation coefficients of single range profile. (c) matrix correlation coefficients $\Delta r = 0$.

20 dB) than the scattering coefficients with HH polarization, and the scattering centers cannot be distinctly observed. (b) represents the correlation coefficients that are obtained via a single range profile correlation. It can be found that the period of the correlation coefficient is sometimes evident, but the corresponding period is not the wobbling period; it is half of the theoretical wobbling period. Although Fig. 4(b) seems to be better than Fig. 3(b), the HV echo of this target will be easily destroyed by noise in the practical application because the scattering field is so weak. (c) is the section plane of the correlation coefficients of **M** at $\Delta r = 0$, and the peak of the correlation coefficient completely corresponds with the wobbling period ($T_w = 1$s), and the wobbling period can be extracted via the matrix correlation.
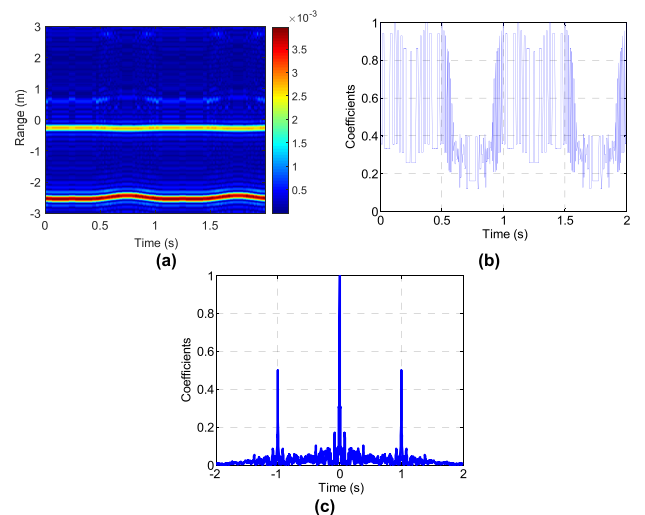

FIGURE 5. Time-range distribution and period estimation, $\gamma_T = 35°$, $\varphi_T = 10°$. (a) time-range distribution. (b) correlation coefficients of single-range profile. (c) matrix correlation coefficients $\Delta r = 0$.

Fig. 5 shows the time-range distribution image and correlation coefficients with the parameters $\gamma_T = 35°$ and

$\varphi_{\mathrm{T}} = 10°$. The period of the correlation coefficient of the range profiles includes three peak values, which do not comprise the wobbling period, as shown in Fig. 5(b), because $\theta_0 \geq 2\psi$ for this condition. However, the correlation coefficient peak of the time-range distribution matrix distinctly corresponds with the wobbling period, which is located at t = 1s. Thus, this proposed method can be employed to estimate the wobbling period for different observation aspects.
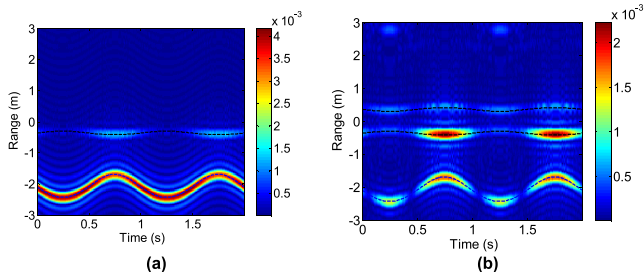

FIGURE 6. Bistatic time-range distribution ($\gamma_{\mathrm{T}} = 35°$, $\varphi_{\mathrm{T}} = 20°$, $\gamma_{\mathrm{R}} = 65°$, $\varphi_{\mathrm{R}} = 140°$). (a) HH polarization. (b) HV polarization.
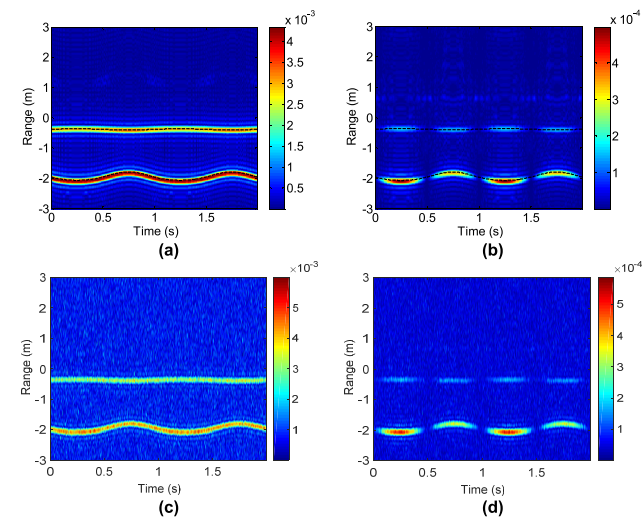
FIGURE 7. Bistatic time-range distribution ($\gamma_{\mathrm{T}} = 35°$, $\varphi_{\mathrm{T}} = 20°$, $\gamma_{\mathrm{R}} = 65°$, $\varphi_{\mathrm{R}} = 20°$). (a) HH polarization. (b) HV polarization. (c) HH polarization with 0 dB SNR. (d) HV polarization with 0 dB SNR.
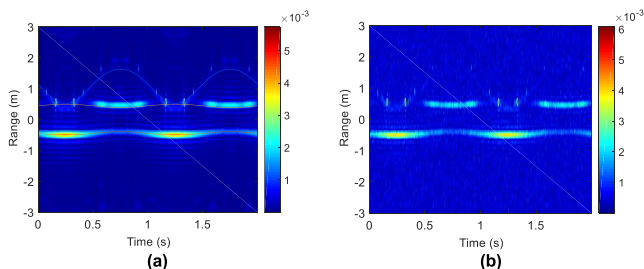

FIGURE 8. Bistatic time-range distribution ($\gamma_{\mathrm{T}} = 140°$, $\varphi_{\mathrm{T}} = 20°$, $\gamma_{\mathrm{R}} = 90°$, $\varphi_{\mathrm{R}} = 60°$). (a) HH polarization. (b) HH polarization with 0 dB SNR.

Figs. 6-8 show the bistatic time-range distribution images with different aspect angles. The dashed lines represent the
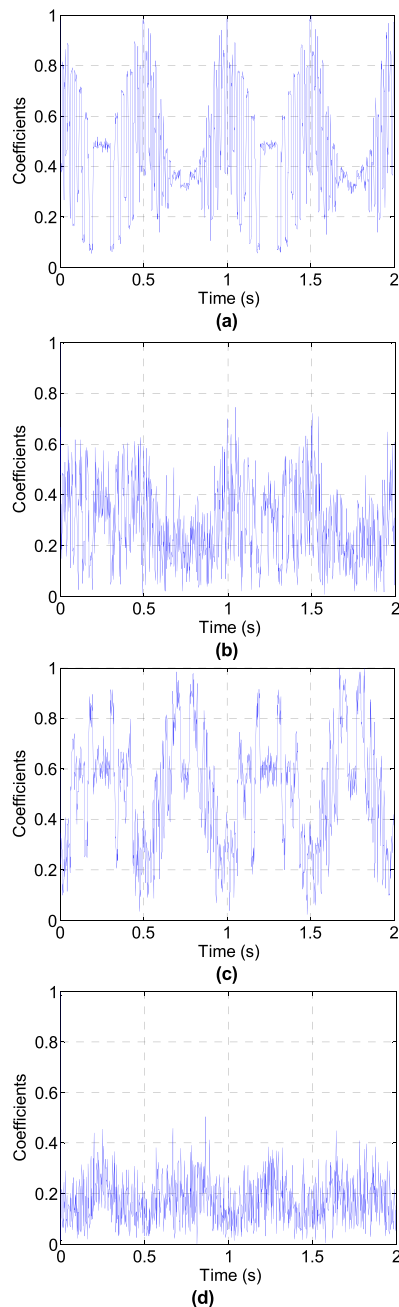

FIGURE 9. Correlation coefficients of single-range profile ($\gamma_{\mathrm{T}} = 35°$, $\varphi_{\mathrm{T}} = 20°$, $\gamma_{\mathrm{R}} = 65°$, $\varphi_{\mathrm{R}} = 20°$). (a) HH polarization. (b) HH polarization 0 dB SNR. (c) HV polarization. (d) HV polarization with 0 dB SNR.

reference distances of the three bistatic scattering centers. The theoretical curves also demonstrate good agreement with the traces of the observed scattering centers. Due to target self-occlusion, only two bistatic scattering centers are observed and the complete characteristics of the target cannot be reflected. In Figs. 6-8: (a) represents the bistatic time-range distribution with HH polarization, and (b) represents the bistatic time-range distribution with HV polarization. The amplitudes of the bistatic HRRPs are almost identical with different receiving polarization, which substantially differs
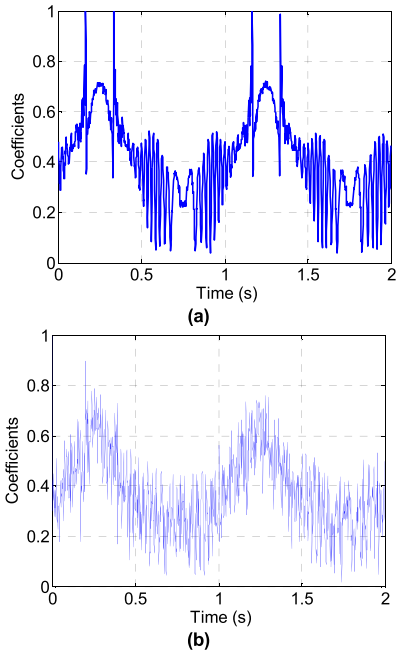
FIGURE 10. Correlation coefficients of single-range profile
($\gamma_T = 140°, \varphi_T = 20°, \gamma_R = 90°, \varphi_R = 60°$). (a) HH polarization. (b) HH
polarization with 0 dB SNR.

from the results in the monostatic radar, where the weak
HV component hinders observation of the scattering center,
as shown in Fig. 4(a). Thus, the dual-polarization receiving
channel will increase the information, which will be useful for
feature extraction. Figs.7(c)(d) and Fig. 8(b) show the bistatic
time-range distribution with WGNs (SNR = 0dB). The weak
scattering centers are concealed by the noise, and the target
feature is destroyed.

Figs. 9~12 show the extracted results of the wobbling
period with different aspect angles. Fig. 9 shows the cor-
relation coefficients of two different range profiles. The
peak value appears in the correlation coefficients at the half
wobbling period with the HH polarizations. For the HV
polarization, the peak values in the correlation coefficients
are irregular due to the fluctuation of the scattering coeffi-
cients. When strong noise is added, the peak value cannot
be observed in the correlation coefficients; thus, the wob-
bling period cannot be extracted, as shown in Fig. 9(b) and
Fig. 9 (d).

Fig. 10 shows the correlation coefficients of the two
different range profiles in Fig. 8. The peak values of the
correlation coefficients do not correspond to the wobbling
period due to some strong scattering characteristics in this
observation aspect; thus, this method for wobbling period
estimation is not robust. Fig. 11 and Fig. 12 display the
section planes of the correlation coefficients of the time-range
distribution matrix at $\Delta r = 0$, and the locations of the peak
values correspond to the wobbling period of 1 s. Even the
SNR is 0 dB, and the peak values are distinctly observed.
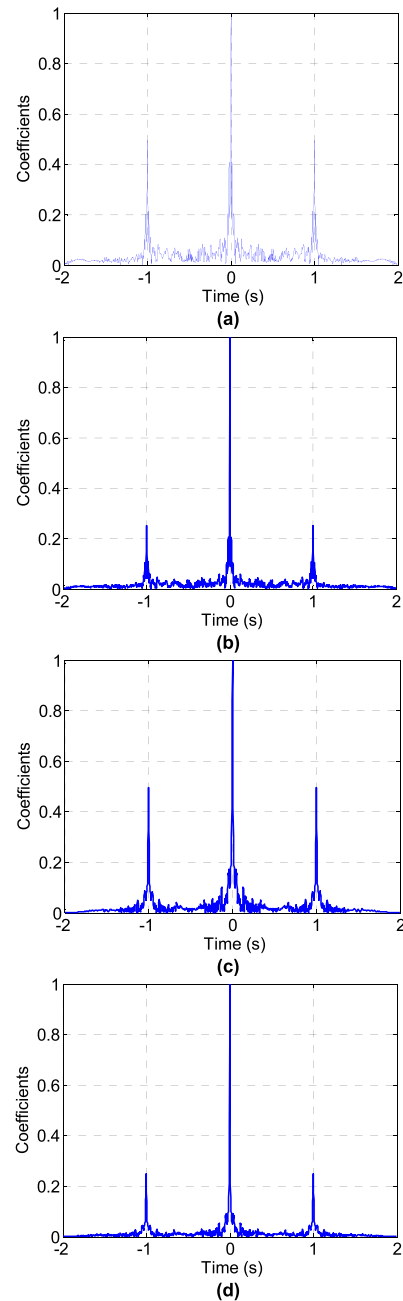It is demonstrated the estimation method of the wobbling

FIGURE 11. Section plane of correlation coefficients of the time-range
distribution matrix ($\gamma_T = 35°, \varphi_T = 20°, \gamma_R = 65°, \varphi_R = 20°$). (a) HH
polarization. (b) HH polarization with 0 dB SNR. (c) HV polarization.
(d) HV polarization with 0 dB SNR.

period via the time-range distribution matrix correlation is
robust.

V. EXPERIMENTAL RESULTS IN ANECHOIC CHAMBER
In this section, the bistatic radar measurement experiments
in anechoic chamber are conducted to verify the effective-
ness of the proposed period estimation method. Because
we have no wobbling targets now, the rotational reflectors
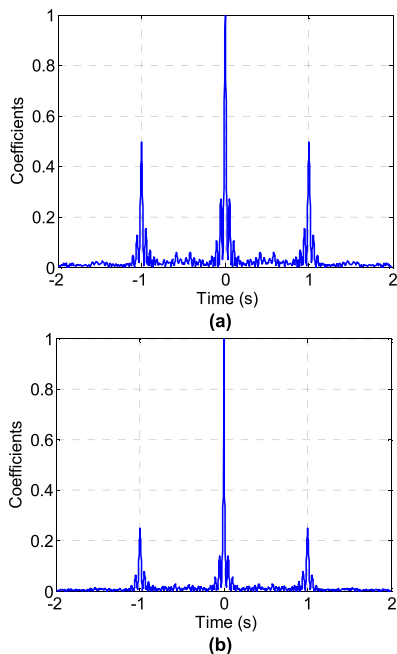are used to simulate the rotational targets with the radius

FIGURE 12. Section plane of correlation coefficients of the time-range distribution matrix($\gamma_T = 140°$, $\varphi_T = 20°$, $\gamma_R = 90°$, $\varphi_R = 60°$). (a) HH polarization. (b) HH polarization with 0 dB SNR.
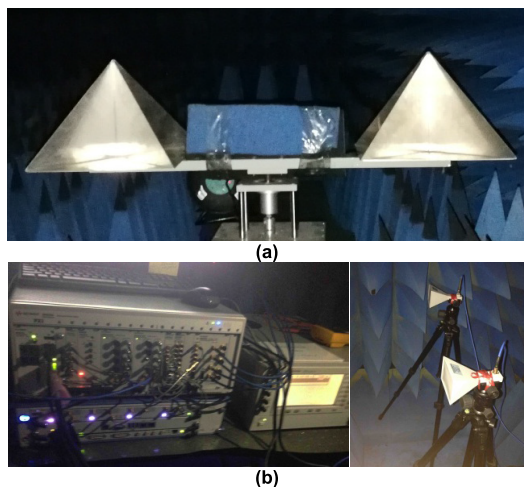

FIGURE 13. Experiment scene and instruments. (a) corner reflectors. (b) experiment system and antenna.

TABLE 1. Experimental parameters.

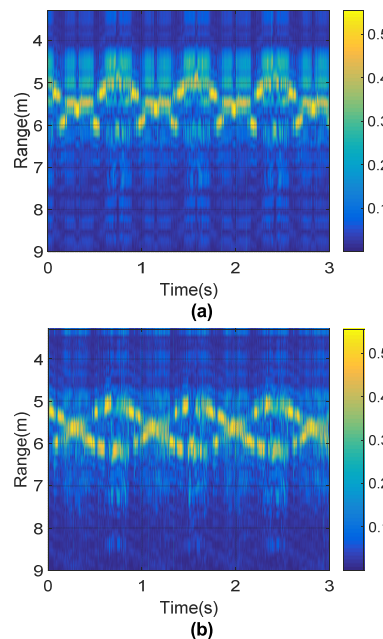| Parameters	Value	Parameters	Value
Carrier frequency	10 GHz	Pulse width	12 μs
Bandwidth	500 MHz	PRF	1000 Hz
Observation time	3 s	Transmitting polarization	H
Receiving polarization	H, V	Bistatic angle	60°
Target length	1.4 m	Rotation frequency	1.2 Hz
Carrier frequency	10 GHz	Pulse width	12 μs

FIGURE 14. Bistatic time-range distribution images. (a)HH polarization. (b)HV polarization.

And the bistatic time-range distribution images as shown in Fig.14. Fig.14(a) represents the bistatic time-range distribution with HH polarization, and Fig.14(b) represents the bistatic time-range distribution with HV polarization. The scattering centers corresponding to the reflectors are observed both in HH and HV polarization channel, and the scattering amplitudes are different. The scattering amplitudes with HH polarization fluctuate violently, while the scattering amplitudes with HV polarization keep stationary.

Fig.15 is the section plane of the correlation coefficients of the time-range distribution matrix at $\Delta r = 0$ with two types of polarization and the peaks of the correlation coefficient correspond to the rotation period are very clear. The rotational period is obtained by peak value detection as 0.835 s (1.198 Hz), which is quite close to the actual value 0.833 s (1.2 Hz). Although the experimental data is obtained in low SNR condition, the rotational periods are also extracted accurately, which validates the robustness of the proposed method.

of 1.4 m as shown in Fig.13 (a). The experiment system are shown in Fig.13(b), which are composed of the general modules such as arbitrary waveform generator (AWG), vector signal generator (VSG), down-conversion (DC) module, intermediate-frequency adjustment module, data acquisition module, and two antennas [22]. The experimental parameters are shown in Table 1.

The transmitting polarization is set as H, while the bistatic receiving polarization is set as H and V. The wideband echo data with two types of polarization are obtained and the bistatic HRRPs are constructed by dechirp processing.
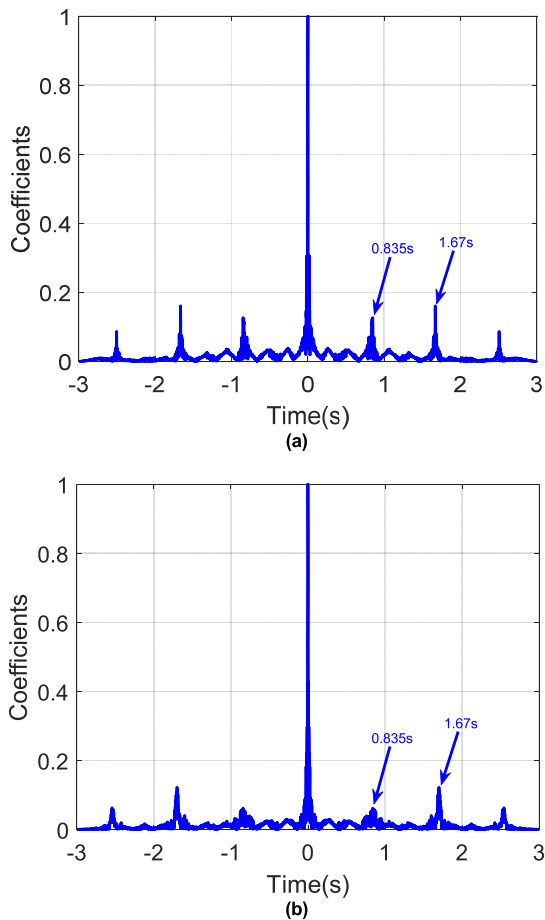
FIGURE 15. Section plane of correlation coefficients of the time-range distribution matrix. (a)HH polarization. (b)HV polarization.

VI. CONCLUSION

The movement model of the bistatic scattering centers of wobbling targets and the wideband bistatic echo model are introduced. The observed HRRP sequence is utilized to construct a time-range distribution matrix, and a robust estimation method of the wobbling period is proposed based on the time-range distribution matrix correlation. Although the wobbling micro-motion is analyzed in this paper, the estimation method is also suitable for other micro-motion, such as rotation and precession, which is validated by experimental data. For the cone-shaped target, in which the HV component is weak in the monostatic radar, whereas the HV and HH components are comparable in the bistatic radar, the dual-polarization receiving channel is suggested for robust feature extraction. Besides, neither the bistatic nor the monostatic configuration can observe all the scattering centers with one observation aspect. Future studies will consider a method for the simultaneous extraction of the target size and wobbling angle via multiple receivers.

REFERENCES

[1] N. J. Willis and H. D. Griffiths, *Advanced in Bistatic Radar*. New York, NY, USA: Scitech, 2007, pp. 1–10.

[2] X. Pan, W. Wang, D. Feng, Y. Liu, Q. Fu, and G. Wang, "On deception jamming for countering bistatic ISAR based on sub-Nyquist sampling," *IET Radar, Sonar Navigat.*, vol. 8, no. 3, pp. 173–179, Mar. 2014.

[3] R. S. A. R. Abdullah, A. A. Salah, A. Ismail, F. H. Hashim, N. E. A. Rashid, and N. H. A. Aziz, "Experimental investigation on target detection and tracking in passive radar using long-term evolution signal," *IET Radar, Sonar Navigat.*, vol. 10, no. 3, pp. 577–585, Mar. 2016.

[4] A. D. Lazarov and T. P. Kostadinov, *Bistatic SAR/GISAR/FISAR Geometry, Signal Models and Imaging Algorithms*. New York, NY, USA: Wiley, 2013, pp. 2–5.

[5] Z. Zhao, X. Zhou, S. Zhu, and S. Hong, "Reduced complexity multipath clutter rejection approach for DRM-based HF Passive bistatic radar," *IEEE Access*, vol. 5, pp. 20228–20234, 2017.

[6] A. R. Persico, C. Clemente, D. Gaglione, C. V. Ilioudis, J. Cao, L. Pallotta, A. De Maio, I. Proudler, and J. J. Soraghan, "On model, algorithms, and experiment for micro-Doppler-based recognition of ballistic targets," *IEEE Trans. Aerosp. Electron. Syst.*, vol. 53, no. 3, pp. 1088–1108, Jun. 2017.

[7] X. Bai and Z. Bao, "Imaging of rotation-symmetric space targets based on electromagnetic modeling," *IEEE Trans. Aerosp. Electron. Syst.*, vol. 50, no. 3, pp. 1680–1689, Jul. 2014.

[8] B. Tang, "Micro-Doppler effect of extended streamlined targets based on sliding scattering center model," *Radio Eng.*, vol. 25, no. 2, pp. 268–274, Feb. 2016.

[9] Y. Luo, Q. Zhang, N. Yuan, F. Zhu, and F. Gu, "Three-dimensional precession feature extraction of space targets," *IEEE Trans. Aerosp. Electron. Syst.*, vol. 50, no. 2, pp. 1313–1329, Apr. 2014.

[10] T. Wang, X. Wang, Y. Chang, J. Liu, and S. Xiao, "Estimation of precession parameters and generation of ISAR images of ballistic missile targets," *IEEE Trans. Aerosp. Electron. Syst.*, vol. 46, no. 4, pp. 1983–1995, Oct. 2010.

[11] H. Gao, L. Xie, and S. Wen, "Analysis and extraction of micro-Doppler induced by cone-shaped target's wobbling," (in Chinese), *Acta Electronica Sinica*, vol. 35, no. 8, pp. 2258–2262, Aug. 2013.

[12] P. lei, K.-L. li, and Y.-X. liu, "Feature Extraction and Target Recognition of Missile Targets based on Micro-motion," in *Proc. IEEE 11th Int. Conf. Signal Process.*, Beijing, China, Oct. 2012, pp. 21–25.

[13] H. Ding and Y. Guan, "Recognition of wobbling and nutating cone-shaped targets," in *Proc. IEEE Int. Conf. Intell. Comput. Intell. Syst.*, Xiamen, China, Oct. 2010, pp. 20–22.

[14] Z. M. Xu, X. F. Ai, Q. H. Wu, "Micro-Doppler characteristics of streamlined ballistic target," *Electron. Lett.*, vol. 55, no. 3, pp. 149–151, Feb. 2019.

[15] X. Bai, F. Zhou, M. Xing, and Z. Bao, "Scaling the 3-D image of spinning space debris via bistatic inverse synthetic aperture radar," *IEEE Geosci. Remote Sens. Lett.*, vol. 7, no. 3, pp. 430–434, Jul. 2010.

[16] G. E. Smith, K. Woodbridge, C. J. Baker, and H. Griffiths, "Multistatic micro-Doppler radar signatures of personnel targets," *IET Signal Process.*, vol. 4, no. 3, pp. 224–233, Jun. 2010.

[17] P. Xia, X. R. Wan, J. X. Yi, and H. Tang, "Micro-Doppler imaging for fast rotating targets using illuminators of opportunity," *IET Radar, Sonar Navigat.*, vol. 10, no. 6, pp. 1024–1029, Jul. 2015.

[18] W. Zhang, C. Tong, and Q. Zhang, "Extraction of vibrating features with dual-channel fixed-receiver bistatic SAR," *IEEE Geosci. Remote Sens. Lett.*, vol. 9, no. 3, pp. 507–511, May 2012.

[19] X. Ai, X. Zou, J. Liu, Y. Li, and S. Xiao, "Bistatic high range resolution profiles of precessing cone-shaped targets," *IET Radar, Sonar Navigat.*, vol. 7, no. 6, pp. 615–622, Jul. 2013.

[20] H.-J. Li, Y.-D. Wang, and L.-H. Wang, "Matching score properties between range profiles of high-resolution radar targets," *IEEE Trans. Antennas Propag.*, vol. 44, no. 4, pp. 444–452, Apr. 1996.

[21] Q. Wang, M. Xing, G. Lu, and Z. Bao, "High-Resolution Three-Dimensional Radar Imaging for Rapidly Spinning Targets," *IEEE Trans. Geosci. Remote Sens.*, vol. 46, no. 1, pp. 22–30, Jan. 2008.

[22] X. Liu, J. Liu, F. Zhao, X. Ai, and G. Wang, "A novel strategy for pulse radar HRRP reconstruction based on randomly interrupted transmitting and receiving in radio frequency simulation," *IEEE Trans. Antennas Propag.*, vol. 66, no. 5, pp. 2569–2580, May 2018.

XIAOFENG AI was born Sichuan, China, in 1983. He received the B.S., M.S., and Ph.D. degrees from the National University of Defense Technology (NUDT), Changsha, China, in 2005, 2007, and 2013, respectively, where he is currently an Associate Professor. His research interests include radar signal processing and feature extraction.

ZHIMING XU was born in Shangdong, China, in 1995. He received the B.S. degree in electronic engineering from Wuhan University, in 2017. He is currently pursuing the Ph.D. degree with the State Key Laboratory of Complex Electromagnetic Environmental Effects on Electronics and Information System (CEMEE), National University of Defense Technology (NUDT), Changsha, China. His research interests include radar imaging technology and radar target recognition.

FENG ZHAO was born in Jiangsu, China, in 1978. He received the B.S. degree in electronic engineering and the Ph.D. degree in information and communication engineering from the National University of Defense Technology (NUDT), Changsha, China, in 2001 and 2007, respectively, where he is currently an Associate Professor. His research interests include radar system design and detection techniques of tracking and guiding radar.

• • •